

PAPER • OPEN ACCESS

## Stripe-yz magnetic order in the triangular-lattice antiferromagnet $\text{KCeS}_2$

To cite this article: Anton A Kulbakov *et al* 2021 *J. Phys.: Condens. Matter* **33** 425802

View the [article online](#) for updates and enhancements.

You may also like

- [Temperature probing and emission color tuning by morphology and size control of upconverting -  \$\text{NaYb}\_{0.67}\text{Gd}\_{0.30}\text{F}\_4\text{:Tm}\_{0.015}\text{Ho}\_{0.015}\$  nanoparticles](#)  
Emille M Rodrigues, Diogo A Gálico, Italo O Mazali et al.
- [Crystal growth and magnetic properties of quantum spin liquid candidate  \$\text{KErTe}\_2\$](#)   
Weiwei Liu, , Dayu Yan et al.
- [Rare-Earth Chalcogenides: A Large Family of Triangular Lattice Spin Liquid Candidates](#)  
Weiwei Liu, , Zheng Zhang et al.



**IOP | ebooks™**

Bringing together innovative digital publishing with leading authors from the global scientific community.

Start exploring the collection—download the first chapter of every title for free.

# Stripe-yz magnetic order in the triangular-lattice antiferromagnet $\text{KCeS}_2$

Anton A Kulbakov<sup>1,2</sup>, Stanislav M Avdoshenko<sup>3</sup>, Inés Puente-Orench<sup>4,5</sup>, Mahmoud Deeb<sup>1</sup>, Mathias Doerr<sup>1</sup>, Philipp Schlender<sup>6</sup>, Thomas Doert<sup>6</sup>  and Dmytro S Inosov<sup>1,2,\*</sup> 

<sup>1</sup> Institut für Festkörper- und Materialphysik, Technische Universität Dresden, 01069 Dresden, Germany

<sup>2</sup> Würzburg-Dresden Cluster of Excellence on Complexity and Topology in Quantum Matter—*ct.qmat*, TU Dresden, 01069 Dresden, Germany

<sup>3</sup> Leibniz-Institut für Festkörper- und Werkstofforschung (IFW Dresden), Helmholtzstraße 20, 01069 Dresden, Germany

<sup>4</sup> Instituto de Nanociencia y Materiales de Aragón (INMA), CSIC-Universidad de Zaragoza, Zaragoza 50009, Spain

<sup>5</sup> Institut Laue-Langevin, 71 avenue des Martyrs, CS 20156, 38042 Grenoble CEDEX 9, France

<sup>6</sup> Fakultät für Chemie und Lebensmittelchemie, Technische Universität Dresden, 01062 Dresden, Germany

E-mail: [dmytro.inosov@tu-dresden.de](mailto:dmytro.inosov@tu-dresden.de)

Received 22 June 2021, revised 9 July 2021

Accepted for publication 19 July 2021

Published 10 August 2021



## Abstract

Yb- and Ce-based delafossites were recently identified as effective spin-1/2 antiferromagnets on the triangular lattice. Several Yb-based systems, such as  $\text{NaYbO}_2$ ,  $\text{NaYbS}_2$ , and  $\text{NaYbSe}_2$ , exhibit no long-range order down to the lowest measured temperatures and therefore serve as putative candidates for the realization of a quantum spin liquid. However, their isostructural Ce-based counterpart  $\text{KCeS}_2$  exhibits magnetic order below  $T_N = 400$  mK, which was so far identified only in thermodynamic measurements. Here we reveal the magnetic structure of this long-range ordered phase using magnetic neutron diffraction. We show that it represents the so-called ‘stripe-yz’ type of antiferromagnetic order with spins lying approximately in the triangular-lattice planes orthogonal to the nearest-neighbor Ce–Ce bonds. No structural lattice distortions are revealed below  $T_N$ , indicating that the triangular lattice of  $\text{Ce}^{3+}$  ions remains geometrically perfect down to the lowest temperatures. We propose an effective Hamiltonian for  $\text{KCeS}_2$ , based on a fit to the results of *ab initio* calculations, and demonstrate that its magnetic ground state matches the experimental spin structure.

Keywords: triangular-lattice antiferromagnets, spin liquids, rare-earth magnetism, *f*-electron systems, rare-earth delafossites, stripe-yz magnetic order, magnetic anisotropy

(Some figures may appear in colour only in the online journal)


## 1. Introduction

In low-dimensional quantum magnets, competing exchange interactions may lead to a strong frustration accompanied by

enhanced quantum fluctuations. Ultimately this can prevent the systems from long-range order, and the ground state is supposed to be a quantum spin liquid (QSL) [1–4]. The theoretically predicted QSL state remains experimentally elusive, and a major ongoing research effort is directed towards the identification of promising QSL candidate materials [5].

Two most promising search directions are pursued. The first is motivated by the seminal work of Kitaev [6] and is focused on materials with anisotropic Kitaev interactions on tricoordinated lattices [7–20]. There is no requirement of geometri-

\* Author to whom any correspondence should be addressed.

 Original content from this work may be used under the terms of the [Creative Commons Attribution 4.0 licence](https://creativecommons.org/licenses/by/4.0/). Any further distribution of this work must maintain attribution to the author(s) and the title of the work, journal citation and DOI.

cal frustration in this case, because the frustration originates from highly anisotropic nearest-neighbor interactions that can result from strong spin–orbit coupling. The most promising candidate compounds in this class are honeycomb-lattice iridates ( $\alpha$ - $\text{Li}_2\text{IrO}_3$ ,  $\text{Na}_2\text{IrO}_3$ ,  $\text{H}_3\text{LiIr}_2\text{O}_6$ ) [7–11] or ruthenates ( $\alpha$ - $\text{RuCl}_3$ ) [14–18] and their three-dimensional polymorphs that form hyper-honeycomb ( $\beta$ - $\text{Li}_2\text{IrO}_3$ ) [12] or stripy-honeycomb ( $\gamma$ - $\text{Li}_2\text{IrO}_3$ ) [13] structures. The difficulty with these model systems is that in real materials, Kitaev interactions coexist with Heisenberg exchange and other possible types of interactions, leading to very intricate magnetic Hamiltonians [20–22]. Existing materials usually end up in different regions of the multidimensional parameter space away from the relatively small theoretically predicted stability regions of the QSL state.

The second search direction rests on the original proposal by Anderson [23] that a QSL ground state can be realized in two-dimensional (2D) spin-1/2 triangular-lattice antiferromagnets (TLAF) as a result of geometrical frustration [24, 25]. The same is true also for other highly frustrated antiferromagnetic (AFM) 2D lattices, such as the kagome lattice [26], which is realized in many copper-containing compounds where quantum spins  $S = 1/2$  reside on the magnetic  $\text{Cu}^{2+}$  ions, most famously in herbertsmithite [27–30]. The difficulty with these systems, however, is that the lattice may experience small structural distortions which are often sufficient to relieve the frustration [30, 31]. Moreover, to the best of our knowledge, no realizations of an undistorted AFM triangular lattice of  $\text{Cu}^{2+}$  spins have been identified to date among inorganic compounds. Therefore, the most suitable materials for the experimental verification of theoretical spin-1/2 models on the triangular lattice are layered rare-earth compounds with  $\text{Ce}^{3+}$  or  $\text{Yb}^{3+}$  ions, characterized by the  $4f^1$  and  $4f^{13}$  electronic configurations, respectively. Whenever the ground-state doublet is sufficiently separated from higher-energy states due to the crystal electric field (CEF) splitting, these ions realize an effective  $\tilde{S} = 1/2$  state at low temperatures. The most studied QSL candidate from this class is  $\text{YbMgGaO}_4$  [32–35], although most recent studies tend to attribute the absence of long-range order in this material to  $\text{Mg}^{2+}$ – $\text{Ga}^{3+}$  site intermixing [36, 37].

A short while ago, a whole new family of compounds with the undistorted triangular lattice of rare-earth ions with little or no structural disorder has been identified [39–42]. These are ternary compounds with the general chemical formula  $A^+R^{3+}X_2^{2-}$ , where  $A$  is an alkali metal (e.g. Na, K, Rb, Cs),  $R$  is a rare-earth ion (in our case, Ce or Yb), and  $X$  is a chalcogen atom (O, S, or Se). They crystallize in the layered delafossite structure depicted in figure 1 that derives from the rock-salt structure upon cation ordering, realizing ABAB-type stacking of magnetic triangular-lattice layers [43, 44]. Low-temperature thermodynamic measurements reveal no signatures of magnetic ordering down to subkelvin temperatures in  $\text{NaYbO}_2$  [39, 45–48],  $\text{NaYbS}_2$  [39, 40, 49], and  $\text{NaYbSe}_2$  [39, 50–52], indicating that these Yb-delafossite compounds may possess QSL ground states. Long-range magnetic order in these systems can be achieved in a moderate magnetic field [47, 50, 53]. On the other hand, their isostructural Ce-based

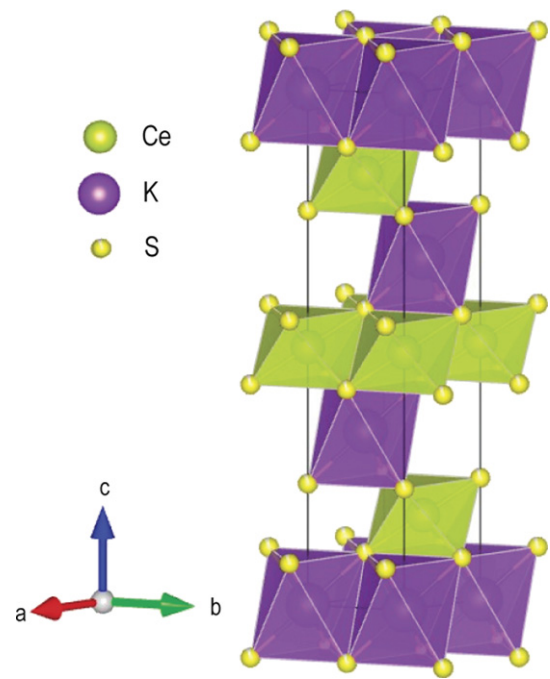


**Figure 1.** Crystal structure of the  $\text{KCeS}_2$  delafossite. The visualization was done in VESTA [38].

counterpart  $\text{KCeS}_2$  develops magnetic order below  $\sim 400$  mK already in zero field, according to the specific-heat data [54].

Because  $\text{Ce}^{3+}$  and  $\text{Yb}^{3+}$  ions have one electron or hole in the  $f$  shell, respectively, and the CEF schemes of all the mentioned compounds have ground-state doublets that are well separated from the excited CEF states [40, 46, 48, 51, 54, 55], one would generally expect the spin-1/2 approximation to be equally applicable to these systems. However, they may still differ in terms of the magnetocrystalline anisotropy and have different eigenfunctions of the CEF ground state with respect to their decomposition in the  $|J, J_z\rangle$  basis, which would place them in different regions of the parameter space of a generic effective Hamiltonian proposed for TLAF [56, 57]. To understand these differences, we have investigated the magnetic structure of the low-temperature ordered phase in  $\text{KCeS}_2$  and its low-temperature lattice structure using powder neutron diffraction.

## 2. Sample preparation

The powder sample of  $\text{KCeS}_2$  was prepared through the following synthesis route. Potassium carbonate and cerium dioxide were mixed in a 20:1 molar ratio and thoroughly ground in a porcelain mortar. A glassy carbon crucible was filled with this mixture and placed in a tube furnace. Before heating up to the target temperature, the whole apparatus including a reservoir for carbon disulfide was flushed with argon for 30 min. The mixture was heated up to  $1050^\circ\text{C}$  within 3 h under an unloaded stream of argon ( $5\text{ L h}^{-1}$ ). While dwelling one hour, a stream of argon of  $0.5\text{ L h}^{-1}$  was used to carry  $\text{CS}_2$  into the hot zone to enable the sulfidization. Finally, the apparatus was allowed to cool down to  $600^\circ\text{C}$  within 6 h and without

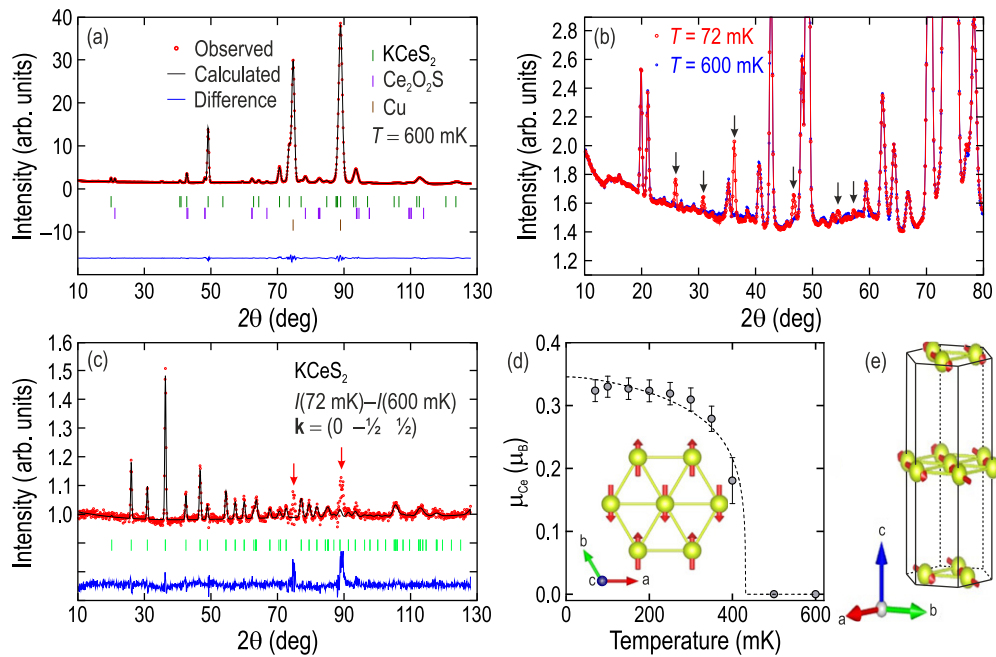


**Figure 2.** Neutron powder diffraction data. (a) Scattered neutron intensity at  $T = 600$  mK as a function of  $2\theta$ , refined in the rhombohedral  $R\bar{3}m$  space group. The fit includes  $\text{Ce}_2\text{O}_2\text{S}$  as an impurity phase and elemental Cu from the sample environment. Green, purple and brown marks denote peaks from  $\text{KCeS}_2$ ,  $\text{Ce}_2\text{O}_2\text{S}$ , and Cu, respectively. (b) Comparison of the scattered neutron intensity measured at  $T = 72$  mK  $< T_N$  (red) and  $T = 600$  mK  $> T_N$  (blue). Black arrows show the magnetic Bragg peaks, which appear below  $T_N$ . (c) The difference of intensities measured at low and high temperatures. Red arrows show the imperfect subtraction of strong Bragg reflections from Cu. (d) Temperature dependence of the magnetic ordered moment. The refined magnetic structure in the  $ab$  plane is shown in the inset. (e) The resulting three-dimensional magnetic structure of  $\text{KCeS}_2$ .

further control down to ambient temperature under a slight argon stream. The ingot that formed in the glassy carbon crucible was then dissolved in water to set the insoluble  $\text{KCeS}_2$  free. Filtering via paper and funnel and washing with water and ethanol produced the sample, mainly composed of intergrown crystals of the target compound and some  $\text{Ce}_2\text{O}_2\text{S}$  as a minority phase. The formation of oxidic by-products during the formation of rare-earth metal chalcogenides (and other compounds of rare-earth metals) is well known and can be attributed to the high oxygen susceptibility of the rare-earth metal ions. It can only be prevented in a completely oxygen-free setup. We also observed that mechanical manipulations (such as pressing, grinding, etc.) can foster decomposition of  $\text{KCeS}_2$  with the formation of the  $\text{Ce}_2\text{O}_2\text{S}$  phase, therefore we avoided grinding the sample and used the as-synthesized powder in neutron-diffraction measurements.

### 3. Powder neutron diffraction

To reveal the spin structure in the low-temperature AFM state of  $\text{KCeS}_2$ , we measured neutron powder diffraction at the D1B high-intensity two-axis powder diffractometer at ILL, France. Neutrons with a calibrated wavelength  $\lambda = 2.5286$  Å were selected with a highly oriented pyrolytic graphite (002) monochromator. The contribution of the instrument to the peaks broadening was determined from the refinement of  $\text{Na}_2\text{Ca}_3\text{Al}_2\text{F}_{14}$  standard sample, while wavelengths were refined using a Si standard. Parasitic diffraction peaks arising from the sample environment were eliminated by a radial

oscillating collimator. Our delafossite sample represented rough powder consisting of small crystallites with lateral sizes up to 0.5 mm. This sample was placed in a Cu can to ensure good thermal contact at subkelvin temperatures and was cooled down using a dilution refrigerator. The measurements were carried out while the sample was rotated about the vertical axis within  $180^\circ$  with a step of  $1^\circ$  (for the 72 and 600 mK datasets) or  $3^\circ$  (other temperatures), with subsequent averaging of the datasets to compensate for the preferred orientations of individual crystallites. The data were collected at several temperatures between 72 and 600 mK in zero magnetic field, allowing for sufficient time for temperature stabilization before every data collection. The measurements at base temperature and at 600 mK were measured with higher statistics, corresponding to approximately 13 h acquisition time per temperature for the 72 and 600 mK datasets.

The 600 mK dataset, collected above  $T_N$ , is plotted in figure 2(a). Apart from the structural reflections from the main  $\text{KCeS}_2$  phase, it contains reflections from the paramagnetic impurity phase  $\text{Ce}_2\text{O}_2\text{S}$  [58, 59], which constitutes about 15% of our sample judging from the results of structural refinement but exhibits no magnetic Bragg reflections. There are also two intense peaks from metallic copper that originate from the sample container, which we included as the third phase. Our Rietveld refinement of the neutron data was done in the assumption of the rhombohedral  $R\bar{3}m$  space group, previously reported for  $\text{KCeS}_2$  from x-ray structure refinement [54, 60]. The agreement between the lattice structures obtained at room temperature and at 600 mK (apart from the

**Table 1.** Low-temperature unit cell parameters,  $\chi^2$  values, and  $R$  factors for our refinement of neutron diffraction data on the majority phase  $\text{KCeS}_2$  and minority phase  $\text{Ce}_2\text{O}_2\text{S}$  at  $T = 72$  and 600 mK. Here  $V$  is the unit cell volume,  $z(\text{S})$  is the  $z$  position of S on the  $6c$  Wyckoff site in  $\text{KCeS}_2$ , and  $z(\text{Ce})$  and  $z(\text{O})$  are the positions of Ce and O on the  $4h$  Wyckoff site in  $\text{Ce}_2\text{O}_2\text{S}$ , respectively.

Parameters	$\text{KCeS}_2$		$\text{Ce}_2\text{O}_2\text{S}$	
	72 mK	600 mK	72 mK	600 mK
Fraction	84.3%		15.7%	
Space group	$R\bar{3}m$ (#166)		$P\bar{3}m1$ (#162)	
Temperature	72 mK	600 mK	72 mK	600 mK
$a$ (Å)	4.2242(1)	4.2243(1)	4.0011(3)	4.0015(2)
$c$ (Å)	21.836(1)	21.836(1)	6.888(1)	6.888(1)
$V$ (Å <sup>3</sup> )	337.44(2)	337.46(2)	95.50(1)	95.52(1)
$z(\text{S})$	0.43(2)	0.43(2)	—	—
$z(\text{Ce})$	—	—	0.28(1)	0.28(1)
$z(\text{O})$	—	—	0.62(1)	0.62(1)
$\chi^2$	2.59	2.45	2.59	2.45
$R_p$ (%)	5.53	5.18	5.53	5.18
$R_{wp}$ (%)	5.66	5.53	5.66	5.53

changes in lattice constants due to thermal expansion) demonstrates the absence of any symmetry-lowering transitions down to  $T_N$ . The low-temperature lattice parameters resulting from the refinement of our neutron data are summarized in table 1.

The magnetic peaks, shown in the 72 mK dataset in figure 2(b) with black arrows, set in below 400 mK—the transition temperature revealed earlier in specific-heat measurements [54]. The difference of the low- and high-temperature datasets, plotted in figure 2(c), contains only magnetic Bragg peaks, whereas the structural scattering from  $\text{KCeS}_2$  and the oxy-sulphide impurity phase is subtracted to zero, which presents strong evidence for the absence of any structural phase transition associated with the magnetic ordering. The commensurate AFM propagation vector  $(0 \frac{1}{2} \frac{1}{2})$  was determined by the  $K\_Search$  algorithm in the FullProf Suite based on difference of the two datasets. Representation analysis carried out with SARAh [61] for the  $R\bar{3}m$  space group with the aforementioned propagation vector suggests two possible common irreducible representations:  $\Gamma_2$  and  $\Gamma_4$ , which we have checked against the temperature-subtracted  $I(0.072 \text{ K}) - I(0.6 \text{ K})$  dataset. Our final result of the magnetic structure refinement, which was done using FullProf Suite [62], is shown in figure 2(c) with a black line. The magnetic signal can be perfectly described only using the  $\Gamma_2$  irreducible representation. Note that the two peaks marked with red arrows are of nonmagnetic origin, as they result from the imperfect subtraction of strong structural reflections from Cu. The magnetic structure of  $\text{KCeS}_2$  is collinear, with spins lying approximately in the  $ab$  plane and pointing orthogonally to the nearest-neighbor Ce–Ce bonds, as shown in the inset to figure 2(d). The refinement suggests a statistically insignificant out-of-plane canting of  $\text{Ce}^{3+}$  spins by  $(5.5 \pm 5)^\circ$ , yet fixing this angle to zero has no significant effect on the quality of the fit, so also the in-plane spin arrangement would be consistent with our data. This type of AFM structure on the triangular lattice is known as ‘stripe- $yz$ ’ order among theorists [56, 57, 63, 64]. The stacking of the AFM

layers along the out-of-plane direction is illustrated in figure 2(e). Note that all magnetic Bragg peaks in figure 2(c) are well described with our model for  $\text{KCeS}_2$ , suggesting that the impurity phase  $\text{Ce}_2\text{O}_2\text{S}$  develops no magnetic order down to 20 mK and could be therefore itself considered a promising spin-liquid candidate.

According to our combined refinement of the magnetic and structural data, the ordered magnetic moment on  $\text{Ce}^{3+}$  at base temperature is approximately  $0.32(1)\mu_B$ . It decreases monotonically with increasing temperature, as shown in figure 2(d), following order-parameter behavior. Fitting this dependence with the empirical function  $\mu(T) = A \tanh[\frac{\pi}{2}(T_N/T - 1)^\alpha]$ , shown with a dotted line, gives a transition temperature  $T_N \approx 430$  mK, which is slightly higher than the value previously observed in thermodynamic measurements [54]. The ordered moment in our data saturates below 300 mK, which may be a consequence of poor temperature stabilization in the powder sample close to the base temperature of the dilution refrigerator. Therefore, it cannot be excluded that we somewhat underestimate the value of the ordered moment at the base temperature.

From the structural refinement of neutron diffraction data, we also obtained the temperature dependence of lattice constants, as it is shown in figure 3 with solid circles. For comparison, we also show our own and previously published cell parameters [60, 65] obtained using x-ray diffraction. Both lattice parameters  $a$  and  $c$  show conventional (positive) thermal expansion above 100 K, whereas below this temperature the thermal expansion is rather small and not measurable within the experimental error. We compare this result with the  $c$ -axis thermal expansion measured by capacitive dilatometry (solid line), carried out using our in-house dilatometer with a sensitivity to relative length changes of about  $10^{-7}$  [66]. The specimen consisted of several flakelike single crystals of  $\text{KCeS}_2$  stacked along the  $c$  axis to achieve a minimum required sample thickness. Therefore, only thermal expansion along the  $c$  axis but not in the  $ab$  plane could be measured. In good agreement with the neutron diffraction data, the capacitive dilatometry confirms a really small thermal expansion below 120 K, where the relative length change is only  $3.5 \times 10^{-4}$ . The linear expansion coefficient  $\alpha$  stays less than  $6 \times 10^{-6} \text{ K}^{-1}$  in this temperature range and only increases noticeably at higher temperatures. Additionally, nearly no magnetostriction could be detected during field sweeps (not shown), where the relative length change is only about  $-1 \times 10^{-5}$  up to 8 T at  $T = 2$  K. The crossover in the behavior of the thermal expansion, observed consistently in diffraction and dilatometry, occurs more than two orders of magnitude higher in temperature than the magnetic ordering transition, which suggests that magnetostrictive effects become effective far above the Néel temperature due to the strong frustration in the system. Moreover, we observe no magnetostriction anomaly at the magnetic ordering temperature (dashed vertical line) in our neutron data. This is another indication that the AFM state is accompanied with no structural distortions, and the delafossite lattice structure with geometrically perfect triangular-lattice layers remains stable even after the stripe- $yz$  AFM order sets in.

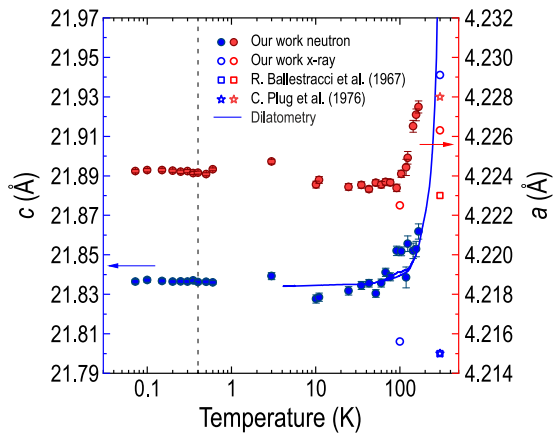


**Figure 3.** Temperature dependence of the  $a$  (red, right scale) and  $c$  (blue, left scale) lattice parameters. Results of the structural refinement of neutron-diffraction data are shown with solid circles. The  $c$ -axis thermal-expansion measurement using capacitive dilatometry is overlaid with a solid line. We also show data points from our own and previously published [60, 65] x-ray diffraction refinement of lattice constants with open symbols for comparison. The error bars are comparable with the point size. The vertical dashed line shows the Néel temperature. Note the logarithmic temperature scale.

## 4. Theory

### 4.1. DFT/PBE/PAW level

We start the theoretical investigation at the density-functional theory (DFT/PBE/PAW) level using VASP suit [67–69]. Admittedly any single-determinant approximation would be a weak one for the  $4f$  system without special arrangements for  $f$ -shell. To deal with the complication due to the  $4f$  shell, at first the  $f$  shell in core potential for Ce is considered [69]. The  $\Gamma$ -centered  $\mathbf{k}$  grid of  $4 \times 4 \times 2$  was used for system optimization and charge density convergence with plane-wave basis cutoff of 400 eV. The original rhombohedral structure has been optimized down to  $10^{-4}$  eV  $\text{\AA}^{-1}$  level with no restrictions on symmetry. The optimized structure preserves the original  $R\bar{3}m$  space group but acquires a slightly expanded unit cell compared to the experimental data,  $a_{th} = 4.23$   $\text{\AA}$  vs  $a_{exp} = 4.22$   $\text{\AA}$  and  $c_{th} = 22.00$   $\text{\AA}$  vs  $c_{exp} = 21.83$   $\text{\AA}$ . While the lattice parameter  $a$  remains within the experimental uncertainty from the measured value, the  $c$  lattice constant experiences a significant (0.78%) expansion along the  $c$  axis, which accounts for  $\sim 0.026$   $\text{\AA}$  expansion of the  $\text{CeS}_6$  trigonal antiprism along the  $C_3$  axis. Nevertheless, the electronic structure is only slightly affected by these differences. Figure 4 shows the band structure profiles along the high symmetry lines of  $\text{KCeS}_2$  with  $4f$  shell in the core and explicit  $4f$ -shell treatment. Expectedly, with  $4f$  electrons in the core,  $\text{KCeS}_2$  represents an indirect-gap semiconductor with large 2.7 and 2.3 eV direct and indirect gaps, respectively, as seen in figure 4(a). Explicit  $4f$ -shell treatment produces a localized state around the Fermi level with a small dispersion driven by  $d$ - $f$  hybridization. At the  $\Gamma$  point, the  $d$ - $f$  hybridization is minimal with a formal gap of  $\sim 0.05$  eV (within the  $f$  shell) and approximately 1.0 eV difference between the populated  $f$  shell and the bottom of

$p$ - $d$  bands at the  $\Gamma$  point. Without alteration of original per-site magnetization, the spin-polarized solution is converged to a ferromagnetic (FM) state as it is indicated by spin density (or magnetization density) in figure 4(c).

Next, we estimate the magnetization energy, using the same DFT level as before, by optimizing a single-determinant wave function for different total magnetization densities:  $\int(\rho_\alpha(r) - \rho_\beta(r))dr = 4$  for the FM state and  $\int(\rho_\alpha(r) - \rho_\beta(r))dr = 0$  for the AFM state. Here, a proper consideration would require a supercell at least accommodating one propagation vector. However, the system of this size will suffer a lot more from well-known DFT shortcomings than a smaller system, and the question of applicability alone would need a separate study. Therefore, here we restrict the consideration to a fragment of a single isolated  $\text{CeS}_2$  layer in a  $2 \times 2$  supercell, as shown in figure 5. We find that thermodynamically the AFM state is more stable than the FM state by 2.0 meV/Ce, as indicated in figures 5(a) and (c). Similar to the complete system, the  $f$  shells form condensed and localized bands around the Fermi level for both spin constraints (see figures 5(b) and (d)). Although the  $f$  shell in the partial density of states (PDOS) has significant rearrangements, the spin density is well localized on the Ce sites and looks very similar before and after the spin flip. Further investigation of the moment orientation will require noncollinear consideration with a spin-orbit coupling Hamiltonian in place. This consideration would, even more, stretch the reliability of the DFT model in its application to  $f$ -shell systems modeling. Moreover,  $4f$  systems have a strictly multiconfigurational character of the ground state  $|J, m_J\rangle$ -multiplet (with  $\hat{H}_{SO} > \hat{H}_{LS}$ ). This cannot be easily accounted for with any DFT model. Multiconfigurational methods such as the complete active space self-consistent field (CASSCF) are generally inapplicable to a periodic system and limited to cluster approximations.

### 4.2. CASSCF(1,7)/RASSI/SO modeling

Luckily, we find our  $f$  shell well isolated in the system. From band structures in figure 4, we find that around the  $\Gamma$  point, the  $4f$  states remain factorized from unoccupied states (lack of  $d$ - or  $p$ -projections and small  $d$  contributions along the  $k$  path). Also, the noticeable contribution of the  $f$  shell to the valance bands is likely an artifact of  $d + p$  and  $f$ -shell projection procedure.

Thus, to understand the local properties, we can restrict our consideration to the local polyhedron (minimal cluster of  $\text{CeS}_6$ ) only. Moreover, as it was shown previously, the local properties of Ce centers in ESR spectra can be rationalized from very simple approximations [54]. Here, we elaborate more on this simple theoretical picture using the full strength of  $^2F_{5/2}$  multiplet modeling based on Stevens parameters predicted through either point-charge models (using MCPHASE [70] program and in-house Python scripts) or the CASSCF(1,7)/ANO-RCC-VDZP/RASSI/SO modeling (with OPENMOLCAS code [71, 72]). We find that apart from some small scaling, both models provide virtually identical results and, for all intents and purposes, can be used interchangeably. We also apply the same level of theory to the impurity

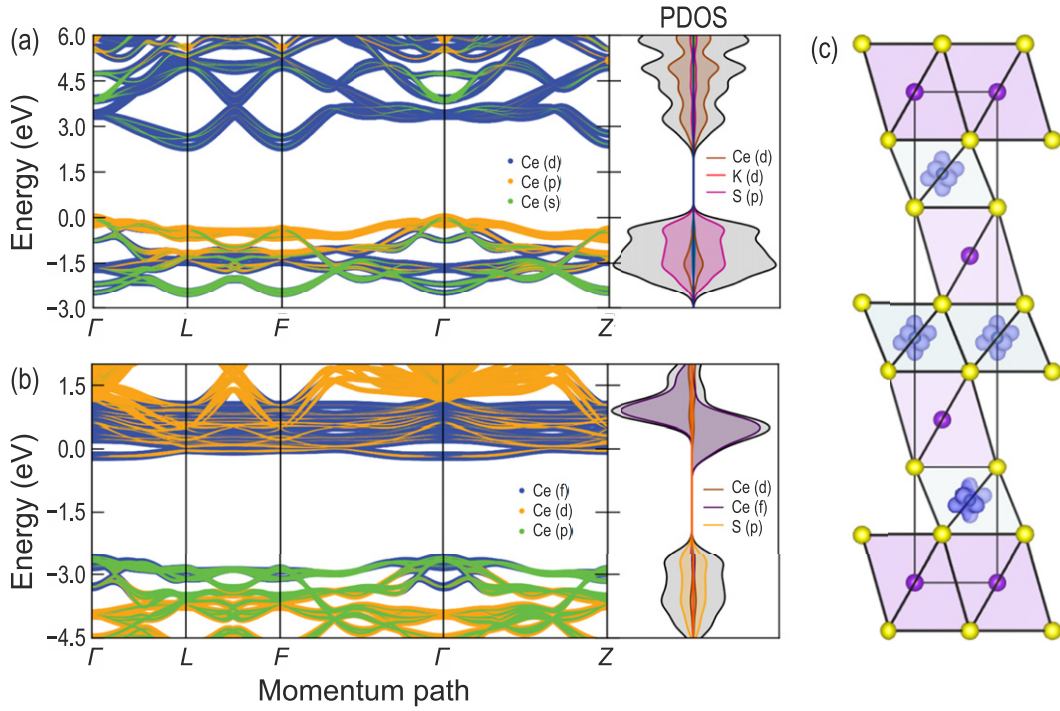


**Figure 4.** DFT/PBE/PAW bands structures and density of states of  $\text{KCeS}_2$  with relevant orbital projections for the  $4f$  shell (a) in the core and (b) with explicit treatment of  $4f$  electrons PAW potentials. (c) The spin density ( $\rho_\alpha - \rho_\beta$ ) for the spin-polarized solution.

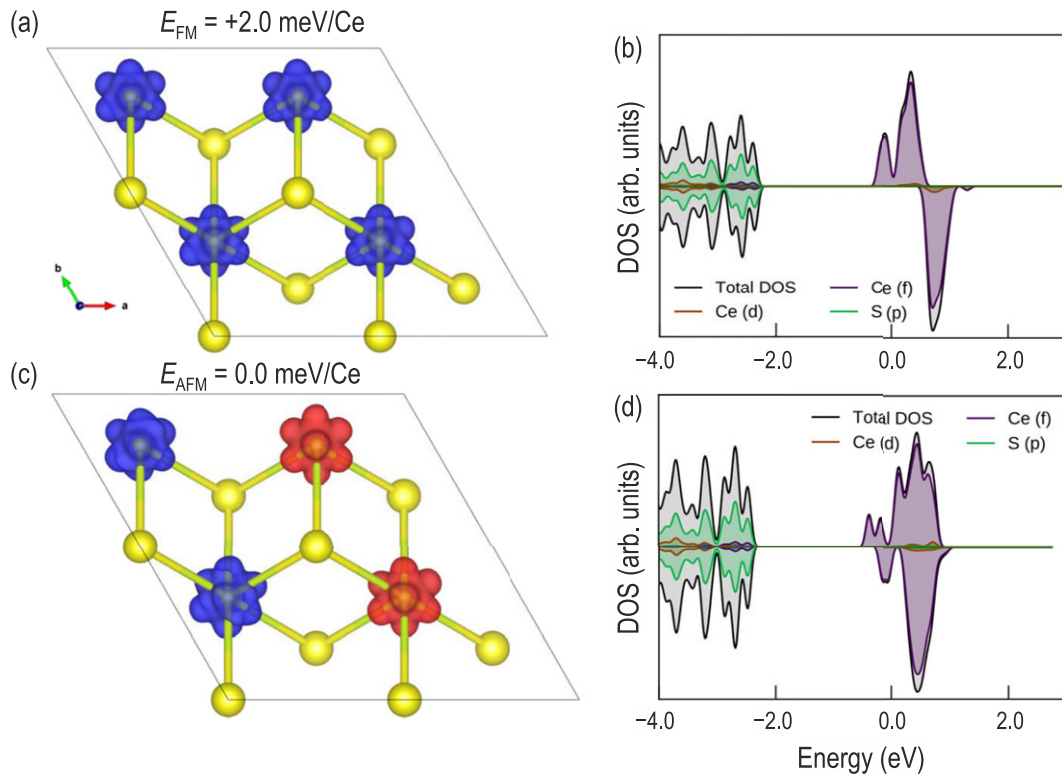
phase  $\text{Ce}_2\text{O}_2\text{S}$  for comparison and better understanding of the experimental results.

Figures 6(b) and (d) show two different projections of the  $\text{CeS}_6$  and  $\text{CeS}_3\text{O}_4$ , respectively, based on the experimentally refined lattice parameters. In the case of  $\text{CeS}_3\text{O}_4$  with an easy-axis anisotropy, the direction of the moment coincides with the direction of the main magnetic axis along  $\mathbf{c}$ . For the ‘easy-plane’ situation in the  $\text{CeS}_6$  cluster, the anisotropy ellipsoid and the radii are given by the  $g$  tensor provided in table 2. Still, it is possible to evaluate total angular momentum components along the main magnetic axis,  $\mu = (\mu_x = \langle 0 | \mathbf{H}_{\text{Zee}} | \mathbf{x} | 0 \rangle = 1.24$ ;  $\mu_y = \langle 0 | \mathbf{H}_{\text{Zee}} | \mathbf{y} | 0 \rangle = 1.24$ ;  $\mu_z = \langle 0 | \mathbf{H}_{\text{Zee}} | \mathbf{z} | 0 \rangle = 0.33$ ). With no external perturbation, this moment has Larmor precession in a plane that is tilted  $10^\circ$  with respect to the  $ab$  plane, which is consistent with the moment canting suggested by the refinement of the magnetic structure from neutron diffraction in section 3.

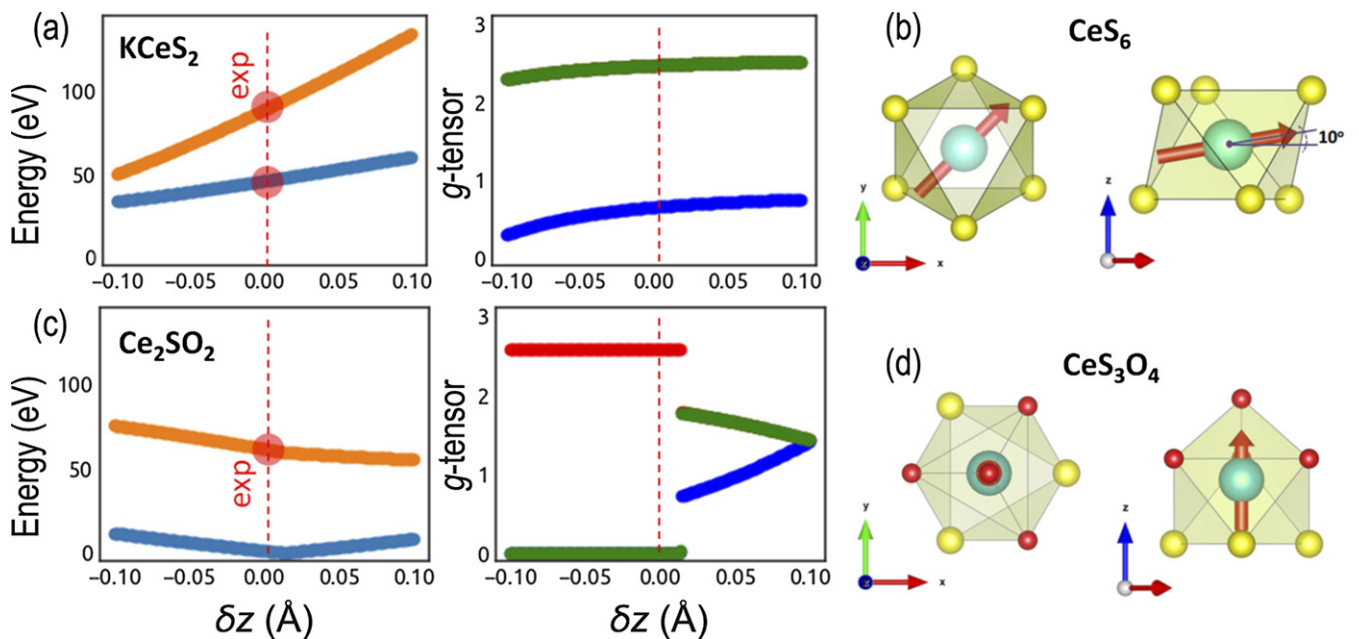
To gain more confidence in the employed theoretical framework, we first studied the impact of the compression/elongation along the  $C_3$ -axis of local Ce polyhedra ( $\text{CeS}_6$  for  $\text{KCeS}_2$  and  $\text{CeS}_3\text{O}_4$  for  $\text{Ce}_2\text{O}_2\text{S}$ ). Figure 6 shows the multiplet transformation (state energies and  $g$  tensor of the ground state) as a function of the elongation  $\delta z$  defined relative to the experimentally refined crystal structure. Interestingly, drastic changes in the state  $g$ -energy diagram are observed within a small deviation of only  $\pm 0.1 \text{ \AA}$  from the experimental value. For example, for  $\text{KCeS}_2$  ( $\text{CeS}_6$  cluster) the energies for the second and third states can change almost twofold and threefold, respectively, in this range. At the same time for  $\text{Ce}_2\text{O}_2\text{S}$  the situation is much more complex. Apart from the pronounced energy change, the system undergoes two local phase

transitions from the easy-axis to easy-plane and back to easy-axis as  $\delta z$  changes from 0.0 to 0.1. The detailed analysis of this phenomenon is outside the scope of this work, so we leave it for follow-up studies. In the following, we compare relative state energies around the experimental geometries and their compositions (table 2).

In our previously published inelastic neutron scattering (INS) data [54], we observed one additional CEF excitation beyond those allowed for the  $\text{Ce}^{3+}$  ion in  $\text{KCeS}_2$ . Such additional CEF lines may arise from an impurity phase [40], from modified local environment due to lattice defects, such as stacking faults [48, 73], or from vibron quasibound states that result from strong magnetoelastic coupling [74, 75]. It is therefore important to verify whether the  $\text{Ce}_2\text{O}_2\text{S}$  impurity phase identified in our present work can account for this additional excitation. In the framework of the point-charge model, we have optimized the S-ion charge at  $q_S = -1.5e$ , so that the first excited state of the  ${}^2F_{5/2}$  multiplet matches the most intense experimental CEF transition at 46 meV, while using the experimental geometries for polyhedral  $\text{CeS}_6$  and  $\text{CeS}_3\text{O}_4$ . In the case of  $\text{CeS}_3\text{O}_4$ , the O-ion point charge is assumed equal to that of the S ion, scaled by the ratio of Hirshfeld population ( $P_O/P_S$ ) predicted by the DFT model:  $q_O = q_S(P_O/P_S) = -1.5e \times 5.0/3.7 \approx -2.0e$ . The calculated intensities of the INS cross section for CEF transitions in both compounds are calculated using the state energies and the wave functions and are given in table 2. Taking the linear combination of the resulting spectra in the proportion  $\text{KCeS}_2:\text{Ce}_2\text{O}_2\text{S} = 85:15$  (corresponding to the results of structural refinement given in table 1), we can reproduce both the energies and intensities of the experimental INS spectrum with remarkable accuracy (see



**Figure 5.** A  $2 \times 2$  supercell of a single  $\text{CeS}_2$  layer with spin density isosurfaces and PDOS as predicted for spin-polarized DFT/PBE/PAW level with ((a) and (b)) FM and ((c) and (d)) AFM spin constraints.



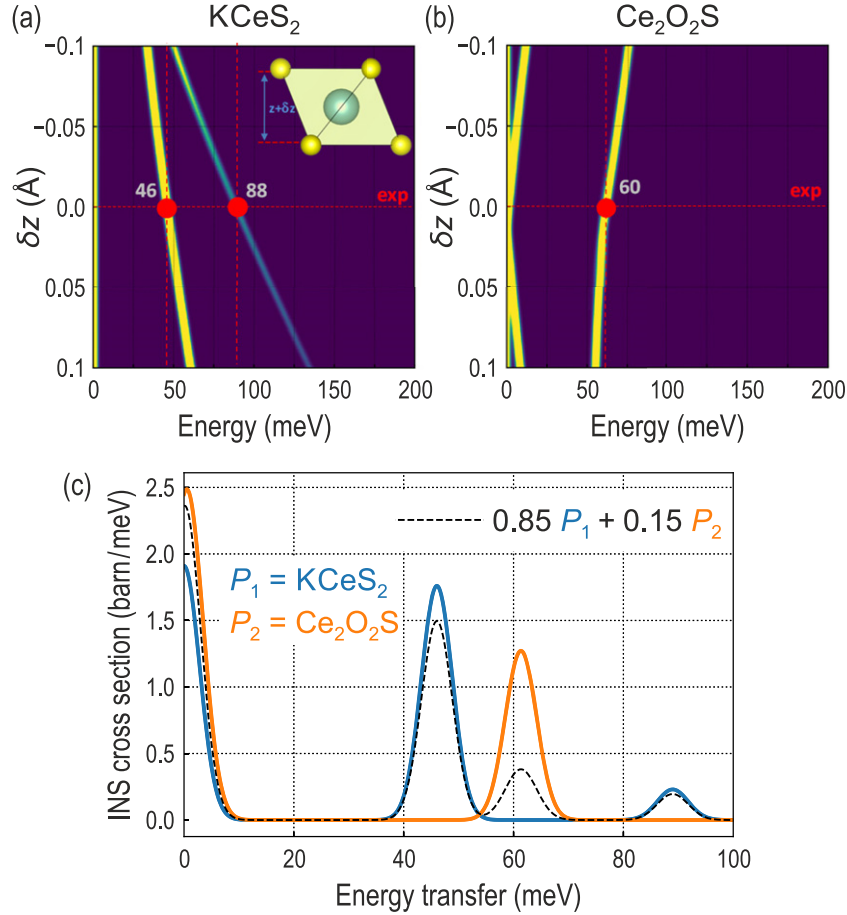
**Figure 6.** ((a) and (c))  $^2F_{5/2}$ -multiplet structure transformation (states energy and the ground-state  $g$ -tensor components) as a function of compression/elongation  $\delta z$ , defined relative to the experimental lattice structure of the (a)  $\text{CeS}_6$  and (c)  $\text{CeS}_3\text{O}_4$  polyhedra along the  $C_3$  axis, obtained from point-charge modeling. ((b) and (d)) The ground-state moment orientation in (b)  $\text{CeS}_6$  and (d)  $\text{CeS}_3\text{O}_4$  clusters.

figure 7). This modeling suggests that the highest-energy peak at 74 meV originates from the  $\text{KCeS}_2$  majority phase, despite its low intensity, whereas the additional peak at 62 meV can be assigned to the oxysulphide phase. As long as the charge

of the ions changes consistently for both phases, the  $\text{Ce}_2\text{O}_2\text{S}$  excitation is always located between the two peaks originating from  $\text{KCeS}_2$ . This leaves no ambiguity in the assignment of the experimental CEF lines.

**Table 2.**  $^2F_{5/2}$  multiplet compositions, wave-function structures in the  $|J, m_J\rangle$  basis, and  $g$ -tensor components for  $\text{Ce}^{3+}$  in the  $\text{CeS}_6$  and  $\text{Ce}_2\text{O}_2\text{S}$  polyhedra with experimental geometry. The last column gives calculated INS cross-sections for the corresponding CEF excitations.

System	Energy (meV)	Wave function	$g_x$	$g_y$	$g_z$	INS, barn
$\text{KCeS}_2$ ( $\text{CeS}_6$ )	0.00	$0.96 \pm 1/2\rangle + 0.04 \mp 5/2\rangle$	2.47	2.47	0.65	1.91
	46.00	$0.97 \pm 3/2\rangle + 0.03 \mp 3/2\rangle$	0.00	0.00	2.57	1.76
	88.98	$0.96 \pm 5/2\rangle + 0.03 \mp 1/2\rangle$	0.1	0.1	4.08	0.23
$\text{Ce}_2\text{O}_2\text{S}$ ( $\text{CeS}_3\text{O}_4$ )	0.00	$0.98 \pm 3/2\rangle + 0.02 \mp 3/2\rangle$	0.00	0.00	2.57	0.81
	3.75	$0.70 \pm 1/2\rangle + 0.30 \mp 5/2\rangle$	1.818	1.818	0.650	1.29
	61.55	$0.70 \pm 5/2\rangle + 0.30 \mp 1/2\rangle$	0.753	0.753	2.780	1.06



**Figure 7.** (a) and (b) 2D regular raster map of INS signals in energy-compression ( $\delta z$ ) coordinates for  $\text{KCeS}_2$  and  $\text{Ce}_2\text{O}_2\text{S}$  at  $T = 10$  K. (c) INS spectra of individual  $\text{KCeS}_2$  ( $P_1$ ) and  $\text{Ce}_2\text{O}_2\text{S}$  ( $P_2$ ) phases with experimental local polyhedron geometries ( $\delta z = 0$ ) and an average spectrum weighted with experimental proportion between  $P_1$  and  $P_2$ .

#### 4.3. The effective Hamiltonian parameterization

To understand the origin of magnetic ordering in  $\text{KCeS}_2$  and be able to compare it with rare-earth delafossites with a quantum-disordered ground state, we need to estimate effective interactions between local moments. The chosen DFT level predicts 2.0 meV/Ce, but this method is notoriously ill-equipped for such tasks. Thus, *ab initio* verifications are needed.

For *ab initio* estimations, however, one has to consider at least two interacting  $\text{Ce}^{3+}$  ions at the same quantum-mechanical level. Fortunately, a pair of  $\text{Ce}^{3+}$  atoms with  $4f^1$  configuration each and an AFM ground state ( $M =$

$2S + 1 = 1$ ) can be described by CASSCF(2,14)/ANO-RCC-VDZP/RASSI/SO problem with just 105 roots (Slater determinants) [71]. This model produces the six low-lying spin orbitals within 60 meV. They comprise a single ground-state singlet, followed by a quasi-doublet at 5.1 meV, an excited singlet at 10.3 meV, and an excited quasi-doublet with an energy of 53.3 meV. For the single  $\text{Ce}^{3+}$ -ion, the *ab initio* ground-state multiplet structure can be reproduced by the minimal  $|J, m_J\rangle$  basis using the derived *ab initio* Stevens parameters,  $B_q^k$ , with 99.98% efficiency [72]. Assuming no significant electronic charge rearrangements ( $\text{Ce}^{3+}$  sites are well-localized) and the Lines model as a valid approximation [76], we can

**Table 3.** Effective interaction parameters of the Hamiltonian (1), obtained by fitting to *ab initio* CASSCF(2,14)/RASSI/SO states energies. The values are given in meV for two different moment models:  $J = 5/2$  and the dipolar moments  $\langle I \rangle$  in MCPHASE [70].

Moment model	$J_{xx}$	$J_{yy}$	$J_{zz}$	$J_{xy}$	$J_{yx}$	$J_{xz}$	$J_{zx}$	$J_{yz}$	$J_{zy}$
5/2	-0.70	-0.60	-4.90	0.0	0.0	0.0	0.0	-0.8	-0.8
$\langle I \rangle$	-0.12	-0.10	-0.81	0.0	0.0	0.0	0.0	-0.13	-0.13

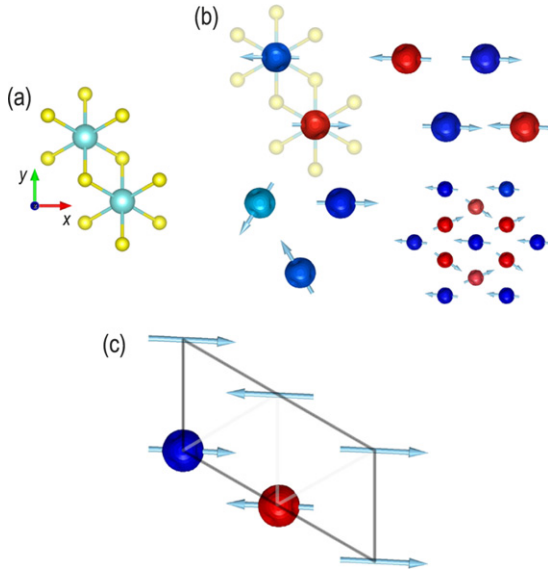


**Figure 8.** (a) Geometry of the two-site model for *ab initio* CASSCF(2,14)/RASSI/SO level calculations. (b) Magnetic order (orientation of the total moments) and on-site  $4f$  charge-density isosurfaces in clusters with 2, 3, 4, and 13 sites. (c) Predicted magnetic unit cell in the  $\text{CeS}_2$  layer and the couplings parameters estimated based in the *ab initio* modeling of the two-sites system (see text for details).

project the two-site *ab initio* solution on the following effective Hamiltonian in the  $|J_1, m_{J_1}; J_2, m_{J_2}\rangle$  basis

$$\hat{\mathcal{H}}_M = \hat{\mathcal{H}}_{\text{CF}_1}(B_q^k) + \hat{\mathcal{H}}_{\text{CF}_2}(B_q^k) - 2 \sum_{\alpha} \sum_{x,y,z} J_{\alpha\alpha} \hat{J}_{\alpha,1} \hat{J}_{\alpha,2} - 2 \sum_{\alpha \neq \beta} \sum_{x,y,z} J_{\alpha\beta} \hat{J}_{\alpha,1} \hat{J}_{\beta,2} \quad (1)$$

in the attempt to retrieve  $J_{\alpha\beta}$  couplings.

Using the Hamiltonian in equation (1), we fit the free parameters  $J_{\alpha\beta}$  to *ab initio* states energies predicted at CASSCF(2,14)/RASSI/SO. We find using the PHI program [77] that the three lowest-energy states can be reproduced exactly with the optimized parameter values given in table 3. Above 15.0 meV, the deviation in energy exceeds tens of meV, presumably due to contributions of the higher-order (multipolar) interactions for which the anisotropic Lines model, with dipolar interactions only, does not account. Moreover, the extracted Hamiltonian is based on the minimal two-site model which lacks the exact crystal symmetry and may overestimate local anisotropy contributions. Nonetheless, this model can describe the four low-lying states including the ground state. Thus, we conclude that this center symmetry model

(figure 8(a)) is able to predict noticeable anisotropy in interactions between local moments and sufficient to control total magnetic order in cluster models. To prove that, these interactions were further implemented in the localized-moments ordering models using the self-consistent mean-field method (see MCPHASE [70] for more details) for clusters of 2, 3, 4, and 13 sites and for fully periodic systems with proper  $q$ -space sampling (figure 8). Having allowed for the  $q$ -sampling and a maximum unit cell up to 4 atoms in any direction, within the proposed interaction Hamiltonian, we obtain from this model the magnetic unit cell shown in figure 8(f). This is consistent with the experimentally observed stripe- $yz$  order and the ordered moment of  $0.33 \mu_B/\text{Ce}$ , which also agrees with the experimental value.

## 5. Discussion and conclusions

In this paper, we have presented the results of magnetic structure refinement for the low-temperature AFM state, which was recently revealed in the effective spin-1/2 triangular-lattice antiferromagnet  $\text{KCeS}_2$ . It represents collinear stripe- $yz$  AFM order with spins lying orthogonal to the nearest-neighbor Ce–Ce bonds in the  $ab$  plane, possibly with a small ( $\sim 10^\circ$ ) out-of-plane canting of the magnetic moments that is also expected from theory. A similar stripe order was recently proposed for the closely related compound  $\text{CeCd}_3\text{As}_3$  [64]. In addition, we have shown that there are no lattice distortions or symmetry-lowering structural transitions associated with the magnetic ordering to within  $\sim 10^{-4}$ . The thermal expansion remains very small ( $\alpha_c < 6 \times 10^{-6} \text{ K}^{-1}$ ) below 120 K, which we confirmed for the  $c$  lattice constant using capacitive dilatometry. Our experimental results also indicate that cerium oxysulphide,  $\text{Ce}_2\text{O}_2\text{S}$ , which was present in our sample as a minority phase, does not order magnetically down to 20 mK and may therefore represent a promising spin-liquid candidate deserving a separate study.

Following the experimental determination of the magnetic structure, we could explain it using first-principles calculations that predict exchange-coupling anisotropy in the pair interaction between two neighboring  $\text{Ce}^{3+}$  ions. This resulting coupling tensor can be regarded as *ab initio* because it was based on a direct fit of low-energy spectra of the exact RASSI/SO problem with no further approximations. We find that only a limited number of spin-orbitals can be used in the fit, which is direct evidence that at higher energy, coupled states are mediated by higher-order couplings beyond dipolar. We also find that, surprisingly, plain-vanilla DFT model at PBE/PAW level with explicit  $4f^1$  treatment correctly predicts the dominance of AFM phase over FM with the reasonable magnetization

density and the difference in energy between AFM and FM configurations of 2 meV/Ce, which is remarkably close to the mean isotropic coupling,  $(J_{xx} + J_{yy} + J_{zz})/3 = 2.1$  meV/Ce.

Furthermore, comparing the ratio of  $J_{ij}$  components in our model with the recent group-theoretical study with a pseudospin-1/2 moment model on a similar lattice [57, 63], we find that with  $J_{yz}/J_{xx} \sim 1$  the KCeS<sub>2</sub> system should be deep in the stripe- $yz$  region of the phase diagram, in consistency with our experimental spin structure.

## Acknowledgments

This project was funded in part by the German Research Foundation (DFG) under the individual research Grant IN 209/9-1, via the project C03 of the Collaborative Research Center SFB 1143 (project-id 247310070) at the TU Dresden, and the Würzburg-Dresden Cluster of Excellence on Complexity and Topology in Quantum Matter—*ct.qmat* (EXC 2147, project-id 390858490). SA thanks A Popov (IFW, Dresden) and M Vojta (TU Dresden) for fruitful discussions and acknowledges financial support from the German Research Foundation (DFG) under Grant No. AV 169/3-1. We also acknowledge V Joyet and S Djellit for technical assistance and Institut Laue-Langevin, Grenoble (France) for providing neutron beam time.

## Data availability statement

The data that support the findings of this study will be openly available following an embargo at the following URL/DOI: [10.5291/ILL-DATA.5-31-2704](https://doi.org/10.5291/ILL-DATA.5-31-2704). Data will be available from 28 September 2025.

## ORCID iDs

Thomas Doert  <https://orcid.org/0000-0001-7523-9313>

Dmytro S Inosov  <https://orcid.org/0000-0003-0639-2503>

## References

- [1] Lacroix C, Mendels P and Mila F (ed) 2011 *Introduction to Frustrated Magnetism* vol 164 (Berlin: Springer)
- [2] Ramirez A P 1994 *Annu. Rev. Mater. Sci.* **24** 453–80
- [3] Greedan J E 2001 *J. Mater. Chem.* **11** 37–53
- [4] Knolle J and Moessner R 2019 *Annu. Rev. Condens. Matter Phys.* **10** 451–72
- [5] Broholm C, Cava R J, Kivelson S A, Nocera D G, Norman M R and Senthil T 2020 *Science* **367** eaay0668
- [6] Kitaev A 2006 *Ann. Phys., NY* **321** 2–111
- [7] Chaloupka J, Jackeli G and Khaliullin G 2010 *Phys. Rev. Lett.* **105** 027204
- [8] Singh Y, Manni S, Reuther J, Berlijn T, Thomale R, Ku W, Trebst S and Gegenwart P 2012 *Phys. Rev. Lett.* **108** 127203
- [9] Yamaji Y, Nomura Y, Kurita M, Arita R and Imada M 2014 *Phys. Rev. Lett.* **113** 107201
- [10] Alpichshev Z, Mahmood F, Cao G and Gedik N 2015 *Phys. Rev. Lett.* **114** 017203
- [11] Kitagawa K *et al* 2018 *Nature* **554** 341–5
- [12] Takayama T, Kato A, Dinnebier R, Nuss J, Kono H, Veiga L S I, Fabbri G, Haskel D and Takagi H 2015 *Phys. Rev. Lett.* **114** 077202
- [13] Modic K A *et al* 2014 *Nat. Commun.* **5** 4203
- [14] Sandilands L J, Tian Y, Plumb K W, Kim Y-J and Burch K S 2015 *Phys. Rev. Lett.* **114** 147201
- [15] Nasu J, Knolle J, Kovrizhin D L, Motome Y and Moessner R 2016 *Nat. Phys.* **12** 912–5
- [16] Banerjee A *et al* 2016 *Nat. Mater.* **15** 733–40
- [17] Banerjee A *et al* 2017 *Science* **356** 1055–9
- [18] Trebst S 2017 Kitaev materials *Topological Matter—Topological Insulators, Skyrmions and Majoranas (Lecture Notes of the 48th IFF Spring School)* vol **139** ed S Blügel, Y Mokrousov, T Schäpers and Y Ando (Jülich: Schriften des Forschungszentrums Jülich GmbH) ch D3
- [19] Gordon J S, Catuneanu A, Sørensen E S and Kee H-Y 2019 *Nat. Commun.* **10** 2470
- [20] Takagi H, Takayama T, Jackeli G, Khaliullin G and Nagler S E 2019 *Nat. Rev. Phys.* **1** 264–80
- [21] Rau J G, Lee E K H and Kee H Y 2014 *Phys. Rev. Lett.* **112** 077204
- [22] Rusnăčko J, Gotfryd D and Chaloupka J 2019 *Phys. Rev. B* **99** 064425
- [23] Anderson P W 1973 *Mater. Res. Bull.* **8** 153–60
- [24] Balents L 2010 *Nature* **464** 199–208
- [25] Li Y, Gegenwart P and Tsirlin A A 2020 *J. Phys.: Condens. Matter* **32** 224004
- [26] Sachdev S 1992 *Phys. Rev. B* **45** 12377–96
- [27] Hermele M, Ran Y, Lee P A and Wen X-G 2008 *Phys. Rev. B* **77** 224413
- [28] Han T-H, Helton J S, Chu S, Nocera D G, Rodriguez-Rivera J A, Broholm C and Lee Y S 2012 *Nature* **492** 406–10
- [29] Han T H, Norman M R, Wen J J, Rodriguez-Rivera J A, Helton J S, Broholm C and Lee Y S 2016 *Phys. Rev. B* **94** 060409
- [30] Norman M R 2016 *Rev. Mod. Phys.* **88** 041002
- [31] Inosov D S 2018 *Adv. Phys.* **67** 149–252
- [32] Li Y *et al* 2015 *Sci. Rep.* **5** 16419
- [33] Li Y, Chen G, Tong W, Pi L, Liu J, Yang Z, Wang X and Zhang Q 2015 *Phys. Rev. Lett.* **115** 167203
- [34] Paddison J A M, Daum M, Dun Z, Ehlers G, Liu Y, Stone M B, Zhou H and Mourigal M 2017 *Nat. Phys.* **13** 117–22
- [35] Kimchi I, Nahum A and Senthil T 2018 *Phys. Rev. X* **8** 031028
- [36] Li Y, Adroja D, Bewley R I, Voneshen D, Tsirlin A A, Gegenwart P and Zhang Q 2017 *Phys. Rev. Lett.* **118** 107202
- [37] Zhu Z, Maksimov P A, White S R and Chernyshev A L 2017 *Phys. Rev. Lett.* **119** 157201
- [38] Momma K and Izumi F 2011 *J. Appl. Crystallogr.* **44** 1272–6
- [39] Liu W, Zhang Z, Ji J, Liu Y, Li J, Wang X, Lei H, Chen G and Zhang Q 2018 *Chin. Phys. Lett.* **35** 117501
- [40] Baenitz M *et al* 2018 *Phys. Rev. B* **98** 220409
- [41] Xing J, Sanjeeva L D, Kim J, Stewart G R, Du M-H, Reboredo F A, Custelcean R and Sefat A S 2020 *ACS Mater. Lett.* **2** 71–5
- [42] Schmidt B, Sichelschmidt J, Ranjith K M, Doert T and Baenitz M 2021 *Phys. Rev. B* **103** 214445
- [43] Ohtani T, Honjo H and Wada H 1987 *Mater. Res. Bull.* **22** 829–40
- [44] Kipp D O and Vanderah T A 1990 *Mater. Res. Bull.* **25** 933–7
- [45] Bordelon M M *et al* 2019 *Nat. Phys.* **15** 1058–64
- [46] Ding L *et al* 2019 *Phys. Rev. B* **100** 144432
- [47] Ranjith K M *et al* 2019 *Phys. Rev. B* **99** 180401
- [48] Bordelon M M, Liu C, Posthuma L, Sarte P M, Butch N P, Pajewski D M, Banerjee A, Balents L and Wilson S D 2020 *Phys. Rev. B* **101** 224427

- [49] Sarkar R, Schlender P, Grinenko V, Haeussler E, Baker P J, Doert T and Klauss H-H 2019 *Phys. Rev. B* **100** 241116
- [50] Ranjith K M et al 2019 *Phys. Rev. B* **100** 224417
- [51] Dai P L et al 2021 *Phys. Rev. X* **11** 021044
- [52] Zhang Z et al 2021 *Phys. Rev. B* **103** 184419
- [53] Xing J, Sanjeeva L D, Kim J, Stewart G R, Podlesnyak A and Sefat A S 2019 *Phys. Rev. B* **100** 220407
- [54] Bastien G et al 2020 *SciPost Phys.* **9** 041
- [55] Zhang Z et al 2021 *Phys. Rev. B* **103** 035144
- [56] Zhu Z, Maksimov P A, White S R and Chernyshev A L 2018 *Phys. Rev. Lett.* **120** 207203
- [57] Maksimov P A, Zhu Z, White S R and Chernyshev A L 2019 *Phys. Rev. X* **9** 021017
- [58] Zachariasen W H 1949 *Acta Crystallogr.* **2** 60–2
- [59] Quezel G, Ballestracci R and Rossat-Mignod J 1970 *J. Phys. Chem. Solids* **31** 669–84
- [60] Plug C M and Verschoor G C 1976 *Acta Crystallogr. B* **32** 1856
- [61] Wills A S 2000 *Physica B* **276–278** 680–1
- [62] Rodríguez-Carvajal J 1993 *Physica B* **192** 55–69
- [63] Steinhardt W et al 2021 Phase diagram of  $\text{YbZnGaO}_4$  in applied magnetic field (arXiv:2105.01790) (unpublished)
- [64] Avers K E, Maksimov P A, Rosa P F S, Thomas S M, Thompson J D, Halperin W P, Movshovich R and Chernyshev A L 2021 *Phys. Rev. B* **103** L180406
- [65] Ballestracci R 1965 *Bulletin de la Société française de Minéralogie et de Cristallographie* **88** 207–10
- [66] Rotter M, Müller H, Gratz E, Doerr M and Loewenhaupt M 1998 *Rev. Sci. Instrum.* **69** 2742–6
- [67] Kresse G and Hafner J 1993 *Phys. Rev. B* **47** 558–61
- [68] Perdew J P, Ernzerhof M and Burke K 1996 *J. Chem. Phys.* **105** 9982
- [69] Kresse G and Joubert D 1999 *Phys. Rev. B* **59** 1758–75
- [70] Rotter M 2004 *J. Magn. Magn. Mater.* **272–276** E481–2
- [71] Aquilante F et al 2020 *J. Chem. Phys.* **152** 214117
- [72] Chibotaru L F and Ungur L 2012 *J. Chem. Phys.* **137** 064112
- [73] Gaudet J et al 2019 *Phys. Rev. Lett.* **122** 187201
- [74] Thalmeier P and Fulde P 1982 *Phys. Rev. Lett.* **49** 1588–91
- [75] Adroja D T, del Moral A, de la Fuente C, Fraile A, Goremychkin E A, Taylor J W, Hillier A D and Fernandez-Alonso F 2012 *Phys. Rev. Lett.* **108** 216402
- [76] Lines M E 1971 *J. Chem. Phys.* **55** 2977–84
- [77] Chilton N F, Anderson R P, Turner L D, Soncini A and Murray K S 2013 *J. Comput. Chem.* **34** 1164–75